Cite This: ACS Nano 2019, 13, 8680-86

Stability of Ligands on Nanoparticles Regulating the Integrity of Biological Membranes at the Nano-Lipid Interface

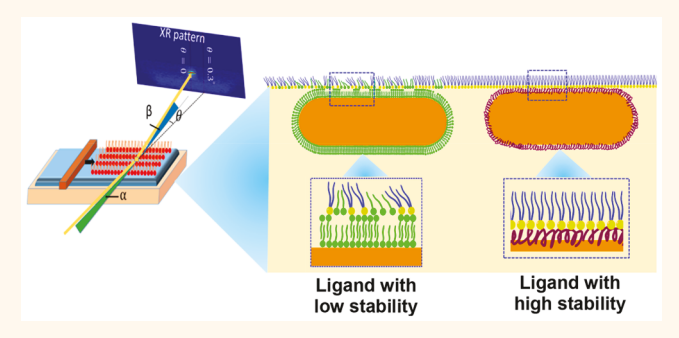
Liming Wang,^{†,#}® Peiyu Quan,^{†,‡,#} Serena H. Chen,^{⊥,#} Wei Bu,[§] Yu-Feng Li,[†]® Xiaochun Wu,^{||} Junguang Wu,^{†,‡} Leili Zhang,[⊥] Yuliang Zhao,[†]® Xiaoming Jiang,[†] Binhua Lin,*,[§]® Ruhong Zhou,*,^{⊥,¶}® and Chunying Chen*,[†]®

[†]CAS Key Laboratory for Biomedical Effects of Nanomaterials & Nanosafety, Institute of High Energy Physics, Chinese Academy of Sciences, and CAS Center for Excellence in Nanoscience, National Center for Nanoscience and Technology of China, Beijing 100049, China

Supporting Information

Downloaded via ARGONNE NATL LABORATORY on September 10, 2019 at 15:40:39 (UTC). See https://pubs.acs.org/sharingguidelines for options on how to legitimately share published articles.

ABSTRACT: When nanoparticles interact with cellular or organelle membranes, the coating ligands are known to affect the integrity of the membranes, which regulate cell death and inflammation. However, the molecular mechanisms of this modulation remain unresolved. Here, we use synchrotron X-ray liquid surface scattering and molecular dynamics simulations to study interface structures between phospholipids and gold nanorods (AuNRs) coated by surfactant and polyelectrolyte. These ligands are two types of widely used surface modification with different self-assembled structures and stabilities on the surface of nanoparticles. We reveal distinct mechanisms of the ligand



stability in disrupting membrane integrity. We find that the cationic surfactant ligand cetyltrimethylammonium bromide detaches from the AuNRs and inserts into phospholipids, resulting in reduced membrane thickness by compressing the phospholipids to align with the shorter ligand. Conversely, the cationic polyelectrolyte ligand poly-(diallyldimethylammonium chloride) is more stable on AuNRs; although it adsorbs onto the membrane, it does not cause much impairment. The distinct coating ligand interactions with phospholipids are further verified by cellular responses including impaired lysosomal membranes and triggered inflammatory effects in macrophages. Together, the quantitative analysis of interface structures elucidates key bio—nano interactions and highlights the importance of surface ligand stability for safety and rational design of nanoparticles.

8680

KEYWORDS: membrane integrity, ligand stability, phospholipid, gold nanorod, X-ray liquid surface scattering

oating ligands affect physicochemical properties of nanoparticles (NPs). 1,2 By tuning type, 3,4 density, 5 composition, 6,7 and chirality 8 of ligands, surface properties of NPs can be well realized, which determine their eventual biomedical effects. When NPs target biological membranes, they will lead to multiple biomedical effects including cellular recognition, the uptake of NPs, 9 inflammation, 10 and cytotoxicity. 11,112 To understand the underlying

causes of these biomedical effects, it is inevitable to investigate nanoparticle—membrane interaction at the interface. Resulting from favorable bioavailability, surfactants and polyelectrolytes

Received: January 6, 2019 Accepted: July 22, 2019 Published: July 22, 2019



[‡]University of Chinese Academy of Sciences, Beijing 100049, China

[§]NSF's ChemMatCARS and Pritzker School of Molecular Engineering, The University of Chicago, Chicago, Illinois 60637, United States

[⊥]IBM Thomas J. Watson Research Center, Yorktown Heights, New York 10598, United States

CAS Key Laboratory of Standardization and Measurement for Nanotechnology and CAS Center for Excellence in Nanoscience National Center for Nanoscience and Technology, Beijing 100190, China

[¶]Department of Chemistry, Columbia University, New York, New York 10027, United States

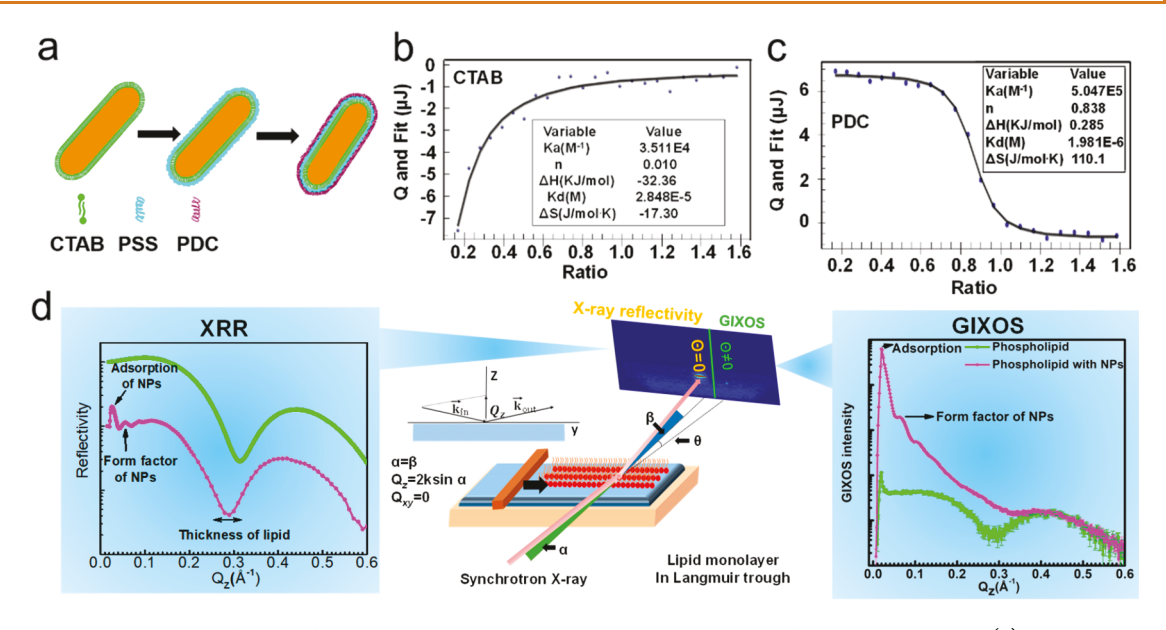


Figure 1. Structure and stability of the surface ligands on Au nanorods and X-ray liquid interface scattering setup. (a) Schematic illustration of the layer-by-layer deposition process of the ligands on the surface of a pristine AuNR. The AuNRs are coated with a CTAB bilayer (CTAB-Au) and then with a layer of the negatively charged polyelectrolyte, PSS (PSS-Au), and finally with the positively charged polyelectrolyte, PDC (PDC-Au). (b, c) Binding affinity of the two kinds of ligands with AuNRs derived from the ITC isotherms of the integrated heat Q at different molar ratios of (b) CTAB and CTAB-Au and (c) PDC and PSS-Au. The data are fit to the standard binding models. Thermodynamic quantities, including association constant (K_a) , dissociation constant (K_d) , stoichiometry (n), and changes in enthalpy (ΔH) and entropy (ΔS) , are listed in the insets. The K_d values reflect the binding affinity between the ligands and their corresponding ligand-coated AuNRs. The sign of the ΔH and ΔS indicates different intermolecular interactions in the two systems. (See the text for more details.) (d) Schematic diagram of the experimental setup for XRR and GIXOS and the scattering geometry shown in the center. A SOPC monolayer (red) is spread on the water (blue) at a surface pressure of 20 mN/m. The two graphs at the left and right are the representative XRR and GIXOS curves illustrating the structures at the AuNR—membrane interface, respectively. The signal at $Q_z \approx 0.06$ Å $^{-1}$ represents the form factor of the rod-like AuNRs and verifies the AuNR adsorption onto SOPC. (See the text for more details.)

are two types of ligands that are widely used for surface functionalization of biomedical NPs.^{7,13,14} Even then, the ligands have distinct assembled structures that exhibit different physicochemical properties within the biological microenvironment.^{13,15} Therefore, it is of great interest to study how ligand structure and stability influence nanoparticle—membrane interactions and to understand the molecular mechanisms behind the distinct inflammatory responses induced by NPs with different surface properties.

Considering the thickness of a phospholipid bilayer, which is 7-8 nm,¹⁶ it is challenging to quantitatively characterize the interface structure at high resolution and high sensitivity in liquid environments. Multiple techniques have been used to study nanoparticle-lipid structure, but it remains difficult to both realize liquid phase measurement^{11,12,17} and obtain quantitative information.^{18–21} To this end, we apply X-ray liquid surface scattering techniques, including X-ray reflectivity (XRR) and grazing incidence X-ray off-specular scattering (GIXOS), 22,23 and molecular dynamics (MD) simulation to quantitatively characterize the interface structure between surface-coated NPs and biological membranes at high resolution. Both XRR and GIXOS are surface-sensitive analytical techniques that provide information in both normal and parallel directions to the surface. Based on the electron density profile of a phospholipid monolayer at the air-liquid interface, the methods allow measurement of the membrane thickness and the amount and the orientation of the NPs adsorbed to the phospholipids.²³⁻²⁶ MD simulations provide detailed molecular structures at the interface and reveal molecular mechanisms of the interaction between NPs and

phospholipids.²⁷ Combining XRR and GIXOS with MD simulations, we are able to capture distinct interactions at the bio—nano interface and quantitatively analyze the biomedical effects of NPs on the structural integrity of biological membranes.

In this study, we used model gold nanorods (AuNRs) to evaluate the biological effects of different coating ligands on membrane structure. AuNRs were coated with two types of ligands, cetyltrimethylammonium bromide (CTAB) and poly-(diallyldimethylammonium chloride) (PDDAC, abbreviated as "PDC"), which both carry a positively charged moiety (CTA and PDDA, respectively) and an anion (bromide and chloride, respectively) but have different self-assembled structures (Figures 1a, S1). CTA molecules form an ordered bilayer structure on the surface of AuNRs (CTAB-Au)²⁸ due to van der Waals (vdW) interactions. In contrast, the PDC layer is relatively disordered, in which PDDA molecules adsorb to AuNRs (PDC-Au) via hydrophobic and electrostatic attraction with negatively charged poly(sodium 4-styrenesulfonate) (PSS).²⁹ The phospholipid 1-octadecanoyl-2-(9Z-octadecenoyl)-sn-glycero-3-phosphocholine (SOPC) is one of the major components in biological membranes. In the X-ray liquid surface scattering experiments, a SOPC monolayer in a Langmuir trough was used to study its interaction with the ligand-coated AuNRs and to characterize the monolayer thickness. The MD simulations demonstrated detailed molecular interactions between the coating ligands of the adsorbed AuNRs and a SOPC bilayer in explicit solvent and elucidated the mechanism of the ligands affecting the thickness of the lipid bilayer. We also evaluated the effects of the internalized ligand-coated AuNRs on

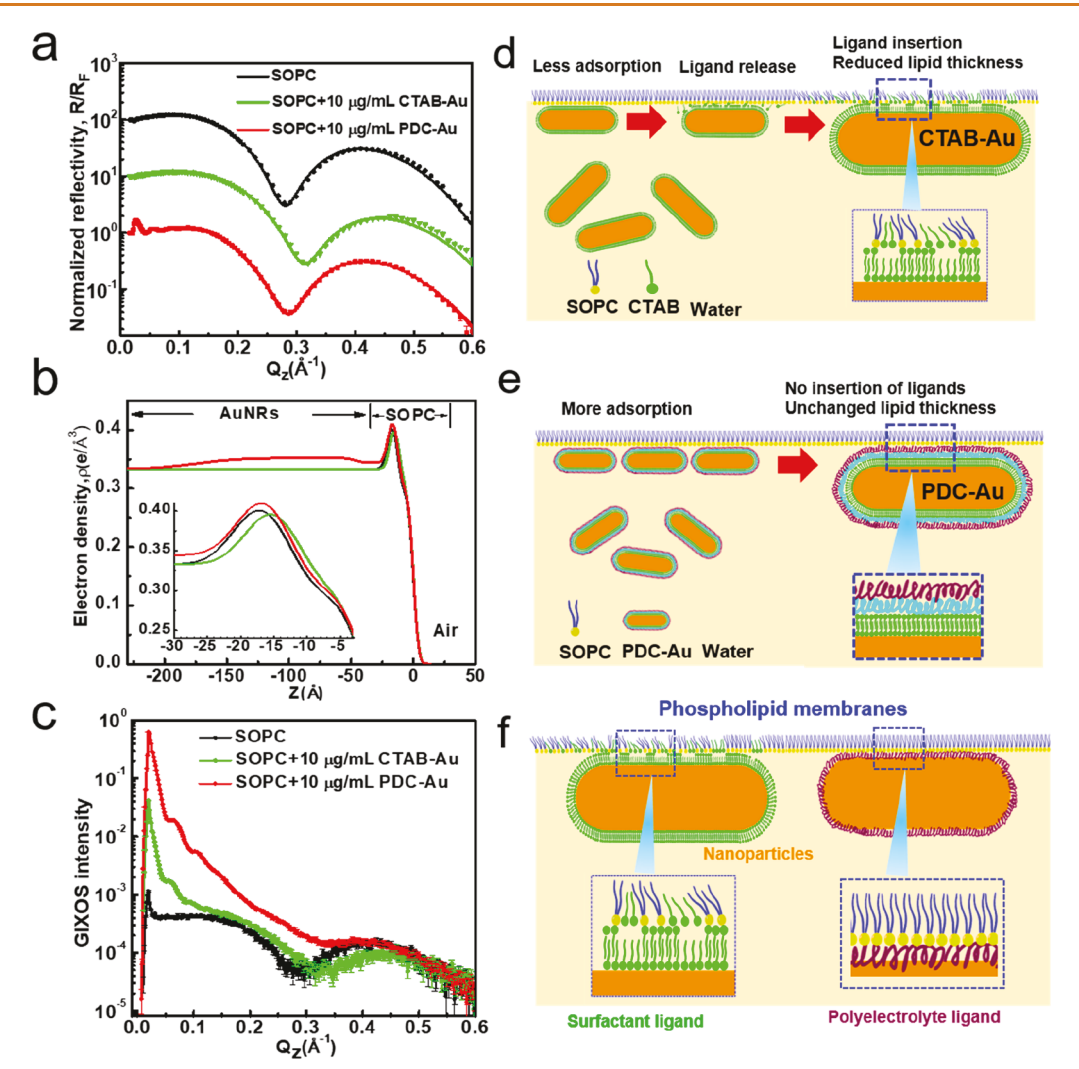


Figure 2. Effect of AuNR adsorption on the SOPC monolayer characterized by XRR and GIXOS and diagrams of the interface structure between AuNRs and the monolayer. (a) XRR data of AuNR adsorption and the SOPC thickness. (b) Electron density profiles derived from the XRR data in (a). (c) GIXOS data of AuNR adsorption onto the SOPC monolayer. The GIXOS intensity reflects the relative amount of the membrane-bound AuNRs. (d, e) Schematic diagrams showing the effect of self-assembled structure and stability of ligands on AuNR adsorption and phospholipid structure. (f) Distinct behaviors of adsorption and ligand insertion for the cationic surfactant- and polyelectrolyte-coated AuNRs when they interact with the lipid monolayer.

the integrity of the cytoplasmic and lysosomal membranes of macrophages. Finally, in the molecular and cellular studies, we explored the inflammatory response induced by the ligand-coated AuNRs, which we found to be associated with the impaired structure of the lysosomal membrane.

RESULTS AND DISCUSSION

Characterization of Ligand-Coated AuNRs. We examined the sizes and surface charges of the prepared CTAB-Au and PDC-Au by transmission electron microscopy (TEM) and zeta potential, respectively. Both AuNRs have a mean diameter of 13.3 ± 1.7 nm and a length of 58.2 ± 2.8 nm and carry positive surface charges (Figure S2). CTA and PDDA have distinct self-assembled structures on the surface of AuNRs. The CTA molecules form an ordered bilayer structure on the surface of AuNRs (CTAB-Au) with a thickness of ~ 32 Å, 15,28 while the PDDA molecules assemble into a relatively disordered layer on the surface of PSS-Au. 29 To probe the stability of the coating ligands, we measured thermodynamic parameters for the Au nanorod—ligand interactions by isothermal titration calorimetry

(ITC) experiments (Figures 1b,c and S3). The parameters derived from the ITC isotherms show negative enthalpy and entropy changes between CTAB and CTAB-Au and positive changes between PDC and PSS-Au. The signs reveal different intermolecular interactions in the two systems, in which the CTA molecules assemble on the surface of CTAB-Au by vdW interactions, while the PDDA molecules assemble through ionic and hydrophobic interactions. Moreover, the dissociation constant (K_d) between CTAB and CTAB-Au is 10-fold greater than that between PDC and PSS-Au, suggesting a higher binding affinity in the latter system.

Thickness Change of Phospholipid Monolayer by Ligand-Coated AuNRs Characterized by X-ray Liquid Interface Scattering. Next, we applied X-ray liquid surface scattering techniques to characterize the structure of a SOPC monolayer and the effect of AuNR adsorption in a Langmuir trough (Figure 1d). We used XRR and GIXOS to derive the electron density profile of the monolayer at the air—liquid interface and calculated the monolayer thickness as well as the amount and the orientation of the NPs adsorbed to the

Table 1. XRR Fitting Parameters for the Structures of the Pure SOPC Monolayer, the AuNR-Bound SOPC Monolayers, and the Ligand-Bound SOPC Monolayers^a

	SOPC	SOPC+ 5 μg/mL CTAB-Au	SOPC+ 10 μg/mL CTAB-Au	SOPC+ 5 μg/mL PDC-Au	SOPC+10 μg/mL PDC-Au	$\begin{array}{c} {\rm SOPC+0.1~\mu g/mL} \\ {\rm CTAB} \end{array}$	SOPC+0.05 μg/ mL PDC
d1 (Å)	$12.8^{1}_{-0.7}$	$12.2_{-1.7}^{1.2}$	$11.6^{0.9}_{-1.1}$	$12.3_{-0.3}^{0.9}$	$12.4_{-0.1}^{1.8}$	$12.3_{-0.8}^{0.9}$	$11.7^{1.1}_{-0.3}$
d2 (Å)	$7.9_{-1.8}^{1.6}$	$7.2^{3.3}_{-2.2}$	$6.9^{2.4}_{-1.9}$	$8.2^{0.2}_{-1.8}$	$8.2^{0.3}_{-1.5}$	$7.1^{1.8}_{-1.8}$	$8.1^{0.9}_{-2.1}$
d1+d2 (Å)	$20.7^{0.9}_{-0.8}$	$19.4_{-1}^{1.6}$	$18.5_{-1}^{1.3}$	$20.5_{-0.3}^{0.3}$	$20.6^{1.8}_{-0.7}$	$19.4_{-0.9}^{0.9}$	$19.8_{-0.8}^{1.2}$
d3 (Å)	N/A	N/A	N/A	$26.1^{1.2}_{-0.1}$	$25.5^{1}_{-1.1}$	N/A	N/A
d4 (Å)	N/A	N/A	N/A	$126.4^{3.3}_{-2.4}$	$132.6_{-1.2}^{1.3}$	N/A	N/A
ho1 (e/Å ³)	$0.292^{0.009}_{-0.007}$	$0.3_{-0.02}^{0.007}$	$0.3^{0.01}_{-0.014}$	$0.294^{0.009}_{-0.012}$	$0.298^{0.01}_{-0.015}$	$0.301^{0.006}_{-0.01}$	$0.294^{0.009}_{-0.005}$
$ ho 2 \left(e/Å^3 \right)$	$0.427^{0.009}_{-0.012}$	$0.429^{0.04}_{-0.029}$	$0.43^{0.039}_{-0.023}$	$0.43^{0.011}_{-0.014}$	$0.433^{0.012}_{-0.022}$	$0.44^{0.036}_{-0.02}$	$0.425^{0.009}_{-0.04}$
ho3 (e/Å ³)	N/A	N/A	N/A	$0.344^{0.001}_{-0.001}$	$0.347^{0.001}_{-0.001}$	N/A	N/A
$ ho$ 4 (e/Å 3)	N/A	N/A	N/A	$0.352^{0.001}_{-0.001}$	$0.364^{0.001}_{-0.001}$	N/A	N/A
σ1, σ2, σ3 (Å)	3.3	3.5	3.4	3.2	3.2	3.4	3.3
σ4 (Å)	N/A	N/A	N/A	5.1	6.8	N/A	N/A
σ5 (Å)	N/A	N/A	N/A	27.9	27.8	N/A	N/A

"d1 and d2 are the thickness of the tail (slab 1) and the head (slab 2) group regions of the SOPC monolayer, respectively. d1+d2 is the overall thickness of the SOPC monolayer. d3 is the distance between the head group region of SOPC and the upside region of AuNR, representing the thickness of the coating ligands on the upside of PDC-Au (slab 3), and d4 is the cross-sectional thickness of the gold region of PDC-Au (slab 4). $\rho1$, $\rho2$, $\rho3$, and $\rho4$ are the electron density of the corresponding area of the slabs. $\sigma1$, $\sigma2$, $\sigma3$, $\sigma4$, and $\sigma5$ represent the root-mean-square roughness of the interfaces between air and slab 1, between slab 1 and slab 2, between slab 2 and slab 3, between slab 3 and slab 4, and between slab 4 and water, respectively. d1, d2, $\rho1$, and $\rho2$ of SOPC with PDC-Au are the standard values of a SOPC monolayer. The large value of $\sigma5$ is due to the polydispersity and the size of PDC-Au *i.e.*, the intrinsic and capillary surface width of AuNRs. The margins of error are calculated using the 95% confidence level.

phospholipids.^{23–26} In the GIXOS curve, a characteristic signal around the wavevector Q_z of 0.06 Å⁻¹ represents the form factor of the Au nanorod. The form factor represents the structural architecture such as the shape, the aggregation state of the nanomaterial, in this case, a nanorod.³¹

The electron density profile of the SOPC monolayer derived from XRR can provide quantitative information on the effect of AuNR adsorption (Figures 2a,b and S4). For instance, exhibiting strong reflectivity, the oscillations at low Q_z on the XRR curve allow the assessment of the relative amount of the adsorbed PDC-Au on the monolayer surface per unit area (Figure 2a). Nevertheless, XRR is less sensitive than GIXOS in detecting adsorbed NPs at the air-liquid interface. The oscillations at low Q_z on the XRR curve were too small to quantify the adsorption of CTAB-Au (Figure 2a), but the form factor (Q_z of 0.06 Å⁻¹) on the GIXOS curve for CTAB-Au exhibits the same width as that for PDC-Au, which verified the adsorption of nanorod-like matter (i.e., CTAB-Au) onto SOPC (Figure 2c). Furthermore, the GIXOS signals at the Q_z value around 0.025 Å⁻¹ indicated the adsorption of both AuNRs. Compared with CTAB-Au, more PDC-Au was adsorbed onto SOPC based on the stronger oscillations on the XRR curve and the higher GIXOS intensity at low Q_z (Figure 2c). The fact that the scattering intensities of PDC-Au are stronger than those of CTAB-Au at the same concentration also suggests that more PDC-Au was adsorbed on SOPC than CTAB-Au (Figure S5c,d).

The reason that PDC-Au and CTAB-Au exhibit a different amount of absorption for SOPC is complex. One reason may be the surface charges of AuNRs. According to the zeta potential, the surface charge of PDC-Au is higher than that of CTAB-Au (Figure S2c), which may result in a greater attractive force between the PO₄³⁻ groups of SOPC and the positively charged moiety of PDC. The other reason may be the stability of the ligands, which we will discuss later.

To calculate the SOPC monolayer thickness from the XRR measurements, we modeled the electron density profiles by a two-slab model.³² For the system of the SOPC monolayer on a

pure water subphase, the fitting data show that the mean thicknesses of the tail group region, the headgroup region, and the SOPC monolayer were $12.8^1_{-0.7}$ Å, $7.9^{1.6}_{-1.8}$ Å, and $20.7^{0.9}_{-0.8}$ Å, respectively. After incubation with $10~\mu g/mL$ CTAB-Au, the corresponding thicknesses decreased and became $11.6^{0.9}_{-1.1}$ Å, $6.9^{2.4}_{-1.9}$ Å, and $18.5^{1.3}_{-1}$ Å, respectively (Table 1). In addition, the wavevector Q_z value corresponding to the minimum of the XRR curve was shifted from $0.28~\text{Å}^{-1}$ to $0.32~\text{Å}^{-1}$, indicating a decrease in the thickness of the SOPC monolayer (Figure 2a). On the contrary, PDC-Au did not affect the thickness of the SOPC monolayer (Table 1, Figure 2a), and the Q_z value corresponding to the minimum of the XRR curve remained the same at different concentrations (Figure SSb).

To explore the underlying factors that cause a decrease in monolayer thickness, we further measured the thickness and area of the SOPC monolayer spread on the pure water with increasing concentration of AuNRs. We found that CTAB-Au causes a decrease of the SOPC thickness in a concentrationdependent manner (Tables 1 and S1). With 5 μ g/mL of CTAB-Au, the Q_7 value corresponding to the minimum of the XRR curve was shifted to 0.3 Å⁻¹ (Figure S5a). The SOPC thickness was $19.4_{-1}^{1.6}$ Å, which was ~ 1.3 Å thinner than that on pure water and ~ 0.9 Å thicker than that with 10 μ g/mL of CTAB-Au (Tables 1 and S1). Moreover, the GIXOS measurements showed that the adsorption of CTAB-Au is concentrationdependent, suggesting different amounts of adsorbed CTAB-Au on the surface of SOPC at the two concentrations (Figure S5c). However, compared to the GIXOS intensities of PDC-Au (Figure S5d), the CTAB-Au intensities were low, which might be due to the interaction between the ligand and lipids at the interface. One possible explanation is that CTA molecules, assembling on the surface of CTAB-Au merely through vdW interactions, detach from the CTAB bilayer and insert into SOPC. To assess this possibility, we measured the surface area of the SOPC monolayer on incremental concentrations of the CTAB-Au subphase at constant surface pressure. By increasing the final concentration of the CTAB-Au subphase, the surface

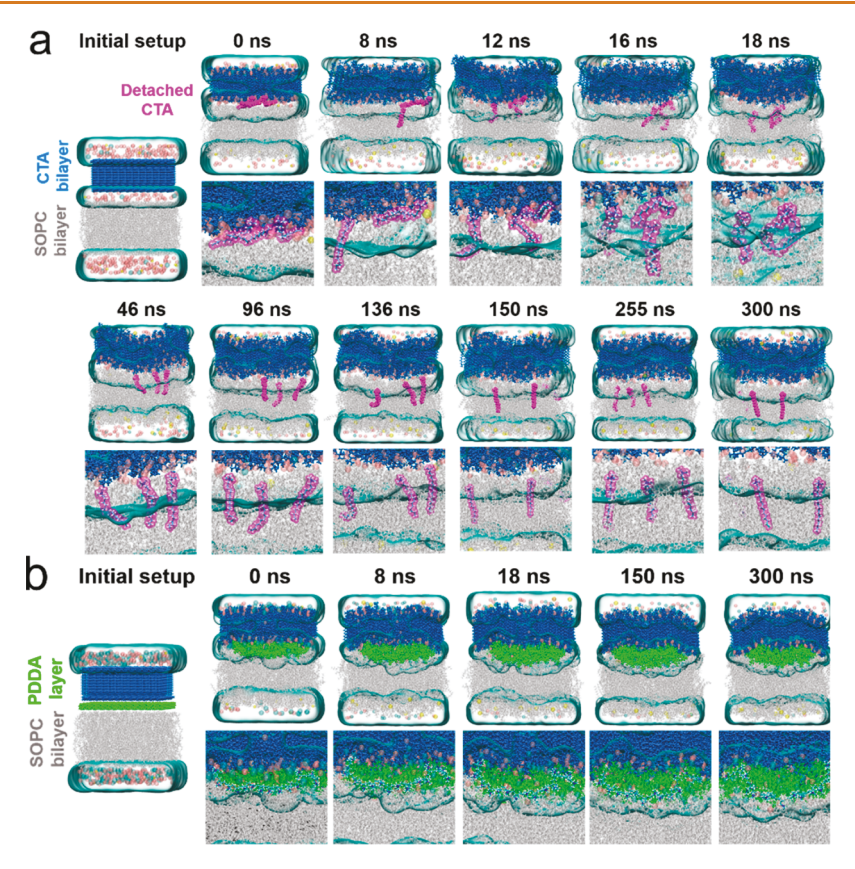


Figure 3. Molecular interaction at the interface between the coating ligands of the adsorbed AuNRs and the SOPC bilayer. Initial system setup and snapshots from a representative trajectory of the (a) CTAB-Au and (b) PDC-Au systems. (a) Three CTA molecules detached from the outer leaflet of the CTAB bilayer and inserted into the outer leaflet of the SOPC bilayer. Once inserted, the CTA molecules diffused in the leaflet. The detached, membrane-inserted CTA molecules are represented as VDW spheres in magenta. (b) The PDDA layer stayed in between the CTAB bilayer and the SOPC bilayer throughout the simulation. The CTAB bilayer is colored in blue, the PDDA layer in green, and the SOPC bilayer in gray. The ions are represented as VDW spheres (Br⁻ in pink, Cl⁻ in cyan, and Na⁺ in yellow). Water is in QuickSurf representation in cyan.

area increased by 5.4, 7.0, and 9.6 cm², respectively (Figure S5e). The increased surface area indicated the insertion of the released CTA molecules into the monolayer, which also explains the lower amount of CTAB-Au adsorption. As we mentioned earlier, the surface charges of AuNRs may result in different amounts of CTAB-Au and PDC-Au absorption for SOPC. Another possible reason may be the release of CTA molecules from the CTAB-Au during the adsorption. As CTA molecules are released from the surface of CTAB-Au and deposited to the space between CTAB-Au and SOPC, they weaken the adsorption of CTAB-Au. In Figures 2d and S5g, we show the schematic diagrams of the adsorption of CTAB-Au on the phospholipids.

More PDC-Au was adsorbed onto the surface of SOPC than CTAB-Au. The amount of PDC-Au adsorbed was also positively correlated with the incubation time and the concentration of PDC-Au (Figures S5b,d and S6). However, unlike CTAB-Au, PDC-Au has a negligible impact on the monolayer thickness (Figures S5b). The surface area of SOPC on the PDC-Au subphase remained quite stable with an increasing concentration of PDC-Au. The surface area increased only by 0.7, 1.3, and 1.9 cm² after incubation with 5, 10, and 20 μ g/mL of PDC-Au, respectively (Figure S5f). The slight change in the surface area might result from the adsorption of PDC-Au and the free PDC. To conclude, during the adsorption of CTAB-Au for the SOPC monolayer, the unstable surfactant ligands may be released from the NPs and insert into the membrane, resulting in a decreased membrane thickness (Figures 2d and S5g). Conversely, more PDC-Au is adsorbed onto the surface of the SOPC monolayer,

but it has a negligible effect on the membrane thickness due to the more stable polyelectrolyte ligands on the surface of AuNRs (Figures 2e and S5h). Figure 2f summarizes the distinct behaviors of adsorption and ligand insertion for the surfactant-and polyelectrolyte-coated AuNRs with cationic charges when they interact with the SOPC monolayer.

With strong reflectivity, the XRR data can also reveal the orientation of the adsorbed PDC-Au. We used a four-slab model to fit the reflectivity data.³² The first two slabs were the same as the two-slab model explained above, where slab 1 was to calculate the average electron density in the tail group region of the SOPC monolayer and slab 2 was to calculate that in the headgroup region. For the additional two slabs, slab 3 was to calculate the average electron density between the headgroup region of SOPC and the upside region of AuNR, representing the coating ligands on the upside of PDC-Au, and slab 4 was to calculate that in the Au nanorod region of PDC-Au. An additional slab was used to calculate the average electron density between the headgroup region of SOPC and the downside region of AuNR. We observed a large roughness between slab 4 and water due to the polydispersity and the size of PDC-Au. 24,26 The best-fit results indicated that the thickness of AuNR (slab 4) was $126.4^{3.3}_{-2.4}$ Å, which was consistent with the mean diameter of the ligand-coated AuNRs in the TEM image, indicating that the long axis of PDC-Au was aligned with the horizontal plane. In addition, the thickness of the coating ligand (slab 3) was $25.5_{-1.1}^{1}$ Å, which also agreed with the approximate thickness of the

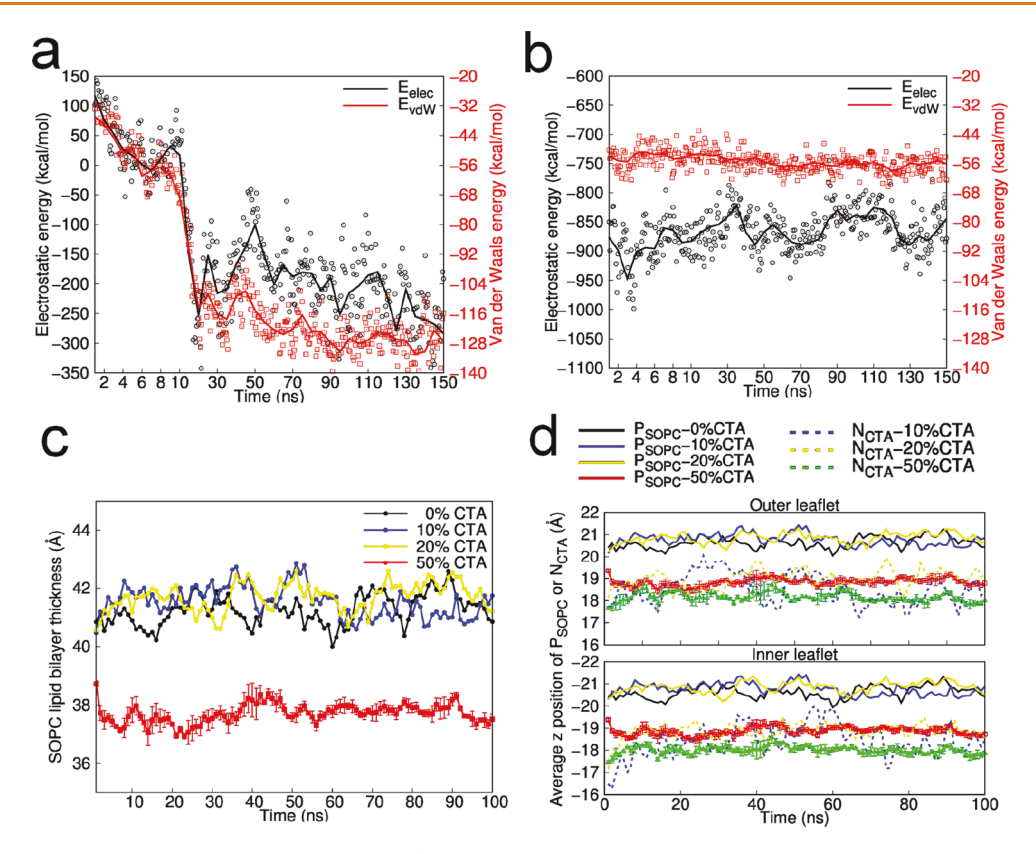


Figure 4. Interaction energies between the coating ligands of AuNRs and SOPC and changes in the membrane thickness by CTA insertion. The electrostatic (black) and vdW (red) interaction energies of SOPC with (a) the three inserted CTA molecules and with (b) one PDDA chain of the PDDA layer in the first 150 ns simulations. Note that the time scale in the first 10 ns is zoomed-in to show the rapid decrease of energies as the detached CTA molecules merged into the lipids. The open circles and squares represent the raw energy data plotted every 0.1 ns before 10 ns and every 0.5 ns afterward. The solid lines are the moving average data in which the raw energy data were averaged every 1 ns before 10 ns and every 5 ns afterward. (c) Membrane thickness of the four heterogeneous membrane systems. (d) Average z positions of the P atoms in SOPC head groups ($P_{\rm SOPC}$, solid lines) and the N atoms in CTA head groups ($N_{\rm CTA}$, dashed lines) in the two leaflets of the four membrane systems. The center of mass of each membrane was set to 0. For the system with 50% inserted CTA, the data are the average of three independent trajectories, and the error bars represent the standard error of the mean.

ligands on the upside of PDC-Au. All XRR fitting parameters are listed in Table 1

Thickness Change of the SOPC Monolayer by Free Ligand Characterized by X-ray Reflectivity. To investigate whether cationic surfactant ligands also affect the SOPC thickness, again we used XRR to characterize the monolayer structure in the presence and absence of the free CTAB and PDC. The 0.1 μ g/mL CTAB was close to the concentration of the free CTAB in the 10 μ g/mL CTAB-Au dispersion and therefore was used as the positive control of the experiment. As expected, the thickness of the monolayer decreased after incubation with 0.1 μ g/mL CTAB (Figure S7a-c). The mean thickness of the tail and the headgroup regions of the monolayer were $12.3_{-0.8}^{0.9}$ Å and $7.1_{-1.8}^{1.8}$ Å, respectively (Table 1). The overall thickness of the monolayer was $19.4^{0.9}_{-0.9}$ Å, which was ~1.3 Å thinner than that on pure water and ~0.9 Å thicker than that on the 10 μ g/mL CTAB-Au subphase (18.5 $^{1.2}_{-1.1}$ Å). The difference between the monolayer thicknesses of the CTAB-Au and CTAB systems suggested that the decreased thickness of the monolayer on the CTAB-Au subphase was due to both the released CTA and the adsorbed CTAB-Au. Moreover, as the concentration of the CTAB subphase increased, the thickness of the monolayer decreased and the surface area increased (Figure S8a-c). The increased surface area indicated the insertion of CTA into the monolayer. Table 1 and Table S1 list the XRR fitting parameters

for the SOPC monolayer on different concentrations of the CTAB subphase.

For PDC, the 0.05 μ g/mL PDC has the same amount of quaternary ammonium groups as that in the 0.1 μ g/mL CTAB and was used as the positive control. Unlike the unchanged thickness of the monolayer on the PDC-Au subphase, the thickness decreased from $20.7^{0.9}_{-0.8}$ Å to $19.8^{1.2}_{-0.8}$ Å on the PDC subphase, suggesting that the free polyelectrolyte ligand caused a decrease in the monolayer thickness. In addition, the thickness decreased as the concentration of PDC increased (Figure S8d,e). Similar to the change in the surface area of the monolayer with CTAB and CTAB-Au, the surface area increased after incubation with PDC, which suggested the insertion of PDC into the monolayer (Figures S7d and S8f). The XRR fitting parameters for the SOPC monolayer on different concentrations of the PDC subphase are listed in Table 1 and Table S2.

Both CTAB and PDC carry positive charges and reduce the monolayer thickness in a concentration-dependent manner. However, the stability of the ligands on the surface of AuNRs has a significant influence on their ability to change the monolayer structure. Based on the $K_{\rm d}$ values, PDC is more stable than CTAB on the surface of AuNRs (Figure 1b,c). Therefore, as PDC-Au adsorbs to the phospholipids, PDC is less likely to detach from PDC-Au or insert into the lipid layer (Figure 2e). On the contrary, CTAB is less stable on CTAB-Au and CTA is

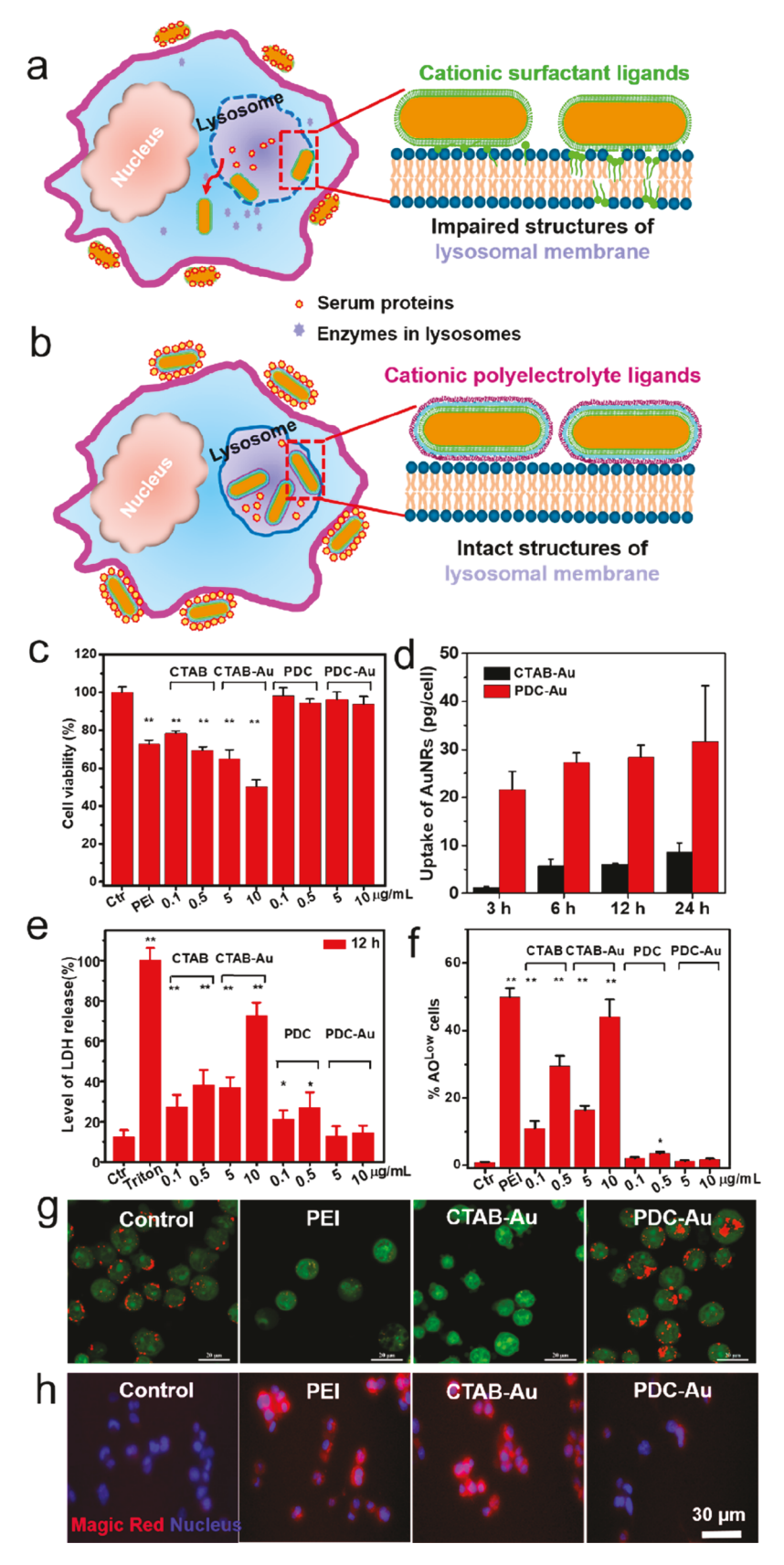


Figure 5. Effects of ligand stability on the membrane integrity and cytotoxicity. (a, b) Schematic diagrams showing how cationic surfactant and polyelectrolyte ligands change the structures of the lysosomal membrane. (c) Viability of THP-1 cells exposed to different concentrations of the ligand-coated AuNRs or the free ligands for 24 h measured by a CCK-8 assay. Unexposed cells were used as the negative control (Ctr), and the cells treated with $2 \mu g/mL$ polyethylenimine (PEI) were used as the positive control. The relative cell viability was expressed as the percentage of the absorbance of the sample relative to that of the negative control. (d) Time-dependent cellular uptake of CTAB-Au and PDC-Au at $10 \mu g/mL$. (e) Change in the cytoplasmic membrane permeability in serum-free media determined by LDH assay. The cells treated with Triton-X100

Figure 5. continued

at a concentration (w/w) of 0.2% were used as the positive control. (f) Change in the lysosomal membrane permeability determined by flow cytometry. The lysosomal membrane permeability was expressed as the percentage of the cells with a low AO fluorescence intensity. (g, h) Assessment of lysosomal membrane integrity after the exposure to CTAB-Au and PDC-Au. (g) THP-1 cells were stained by AO and observed by confocal microscopy. Red fluorescence represents intact endosomes/lysosomes at acidic pH. When the integrity of the lysosomal membrane decreases and pH increases, the intensity of red fluorescence weakens and becomes dominated by green fluorescence. Scale bar: $20 \mu m$. (h) THP-1 cells were stained by Magic Red and Hoeschst 33342 (blue for the nucleus) and observed by fluorescence microscopy. Red fluorescence indicates the release of the lysosomal cathepsin B to the cytoplasm, suggesting damage of the lysosomal membrane. Scale bar: $30 \mu m$. (c-f) Data are the average of four independent replicates. Error bars represent the standard errors. The significant difference between the sample and the control at p < 0.05 is indicated by a single asterisk, and that at p < 0.01 by a double asterisk.

likely to detach from the CTAB bilayer and intercalates into the lipid layer. As a result, the lipid structure is affected when CTAB-Au adsorbs to the phospholipids (Figure 2d).

MD Simulations of the Interactions between Coating **Ligands and SOPC.** To further understand the molecular mechanism at the interface, we used MD simulations to study the structural details of the interactions between the adsorbed AuNRs and a SOPC bilayer. We performed 12 independent MD trajectories to study the interaction between CTAB-Au and a SOPC bilayer. Six of the trajectories started with an initial structure in which the CTAB bilayer was placed closer to the SOPC bilayer along the z-axis. In two of the six trajectories, we observed one CTA molecule that detached from the CTAB bilayer and inserted into the lipids from 1 and 133 ns, respectively (Figure S9 and Movie 2). The other six trajectories began with a structure in which the CTAB bilayer was slightly more distant from the lipid bilayer. Out of the six trajectories, four had one CTA molecule and one had three CTA molecules detaching from the CTAB bilayer (Figure 3a and Movie 1) and merging into the lipids within 20 ns. The distance between the two bilayers provided space for the CTA molecules either (i) to detach from the outer leaflet of the CTAB bilayer, which was facing water, and then to insert into the outer leaflet of the membrane as we saw in Figure 3a and Movie 1, or (ii) to detach from the inner leaflet of the CTAB bilayer, which was facing AuNR, and then to insert into the inner leaflet of the membrane in the periodic image at the +z direction, as we saw in Figure S9 and Movie 2 because we did not constrain the inner leaflet of the CTAB bilayer in the simulations. In reality, AuNRs should constrain the movement of the CTA molecules in the inner leaflet such that they have no access to the membrane. In the simulations, we intended to examine the preferred movement of the released CTA molecules and therefore did not apply constraints to them. Interestingly, the detached CTA molecules preferred to insert into the membrane in the periodic image more than to fall back to the inner leaflet of the CTAB bilayer. Nevertheless, case (ii) happened less frequently. Only one out of the seven trajectories with CTA insertion belonged to case (ii), and the insertion occurred later in time (from 133 ns) (Figure S9). In contrast, PDDA molecules in the PDC-Au system were more stable. In all six trajectories we performed, the PDC layer stayed in between the CTAB bilayer and SOPC throughout the simulations (Figure 3b and Movie 3).

To analyze the effect of the CTA molecule in the SOPC bilayer on the lipids, we calculated the electrostatic and vdW interaction energies between the inserted CTA and the lipids in the seven trajectories that had inserted CTA molecules. Both interaction energies decreased when the CTA molecules merged into the membrane, and the insertion of one CTA molecule corresponded to a $-40~\rm kcal/mol$ decrease in the vdW interaction energy. The trajectory with insertion of three CTA

molecules that we displayed in Figure 3a shows a decrease of 120 kcal/mol in the vdW interaction energy (Figure 4a). On the other hand, the interaction energies of the PDC-Au system remained quite stable (Figure 4b).

To assess the effect of the inserted CTA molecules on the thickness of the SOPC bilayer, we constructed heterogeneous membrane model systems of a SOPC bilayer with 0%, 10%, 20%, and 50% inserted CTA. For each of the four systems, we characterized the thickness of the lipid bilayer by two different methods. One method measured the distance between the average z position of the phosphorus atoms of the lipids in the two leaflets.³⁴ The thickness of the lipid bilayer decreased, especially with a higher concentration of CTA. With 50% inserted CTA, the bilayer thickness decreased from 41 Å to 38 Å (Figure 4c). The other method measured the water density along the z-axis. We defined the thickness of one leaflet of the SOPC bilayer to be the distance between 0 and 1/3 of the maximum water density. With 50% inserted CTA, the thickness of one leaflet decreased from 21.5 Å to 19.5 Å (Figure S10), which agreed very well with the XRR measurements of the SOPC monolayer thickness. Further analysis of the headgroup positions of SOPC and CTA revealed that with a higher concentration of inserted CTA the headgroup positions of the lipids became lower, aligning with the headgroup positions of the inserted CTA (Figure 4d). Together, the inserted CTA molecules affect the membrane structure and decrease its thickness. It is worth mentioning that differences exist in the physical structures of the monolayer and bilayer of SOPC. The bilayer is symmetrical, in which the hydrophobic tails are buried inside and the hydrophilic heads are facing the aqueous phase. On the contrary, the monolayer is asymmetrical, in which the hydrophobic tails are facing the air while the hydrophilic heads are distributed in the water. However, both the monolayer and bilayer of SOPC are similar at the lipid-water interface, where the ligands of AuNRs adsorb and interact. This similarity supports the interface comparison between the AuNRs-SOPC monolayer by X-ray experiments and the AuNRs-SOPC bilayer by the simulations.

Stability of the Ligands on AuNRs Modulating Cell Viability and Membrane Integrity. Next, we verified the influence of ligand stability of NPs at the cellular level. In Figure 5a and b, the surface of NPs is immediately coated by serum proteins to form a protein corona—NP complex. Serving as a physical barrier, the coatings of the protein corona change the surface properties of NPs and prevent the cell membrane from directly contacting with the surface ligands of NPs. 11,12 The complex is then internalized by cells, trapped in the vesicles, and transported to endosomes and lysosomes. In these organelles, the coating proteins will detach from the surface of NPs and the ligands on the surface can contact the lysosomal membrane. As a result, the NPs coated by cationic surfactant ligands impair and

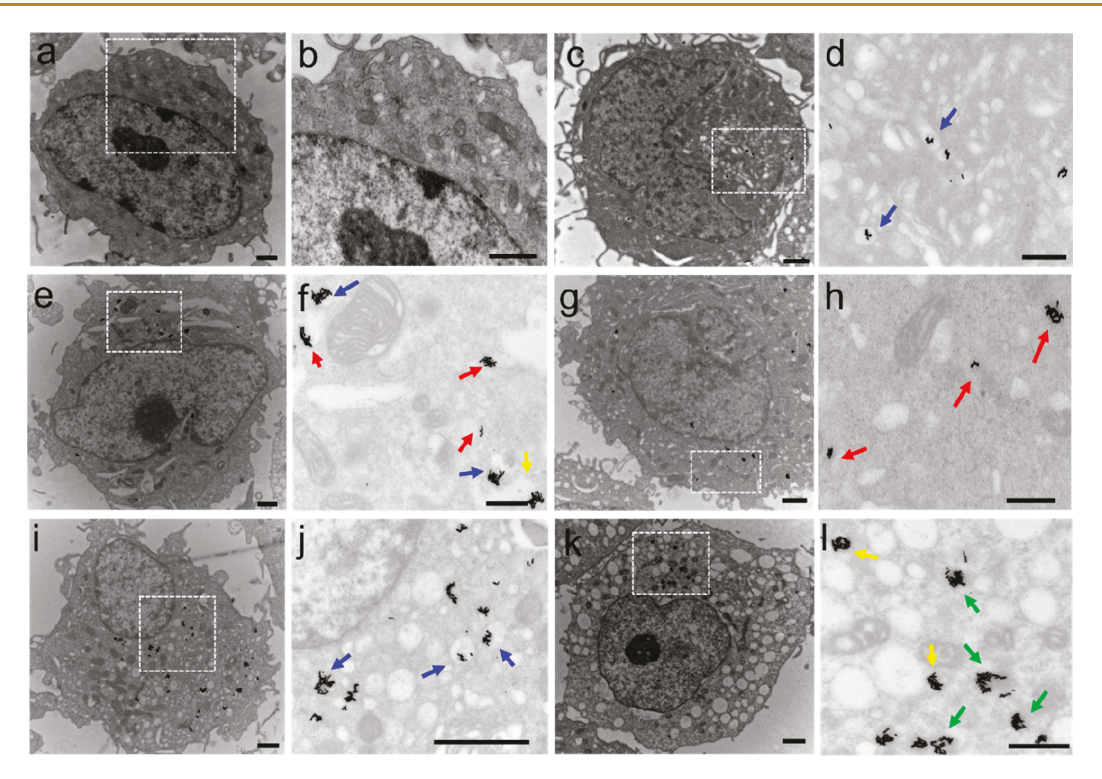


Figure 6. Intracellular localization of CTAB-Au and PDC-Au by TEM imaging. (a,b) TEM images of control cells. (c,d;e,f;g,h) Representative TEM images showing the locations of AuNRs after incubation with CTAB-Au for 3 h (c,d), 6 h (e,f), and 24 h (g,h), respectively. (i,j;k,l) Representative TEM images showing intracellular AuNRs after incubation with PDC-Au for 6 h (i,j) and 24 h (k,l), respectively. (b,d,f,h,j,andl) Zoom-in images of the insets of a, c, e, g, i, and k, respectively. The arrows in blue, green, and yellow denote the AuNRs in the endosomes, lysosomes, and phagosomes, respectively. The red ones show the AuNRs in the cytoplasm. Scale bar: $1 \mu m$.

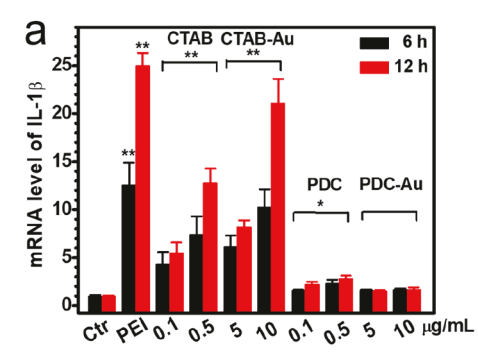
penetrate the lysosomal membrane and then are released in the cytoplasm, which induced inflammation. Conversely, the NPs with polyelectrolyte coatings remain in the lysosome due to negligible effects on the membrane. In these cases, it is improper to observe the effects of ligand stability on the cytoplasmic membrane structure in the presence of serum proteins. Herein, we focus on how the ligand properties of the intracellular NPs affect the lysosomal membrane.

In detail, to study the effects of AuNRs on biological membranes at the cellular level, we used macrophages as a model to evaluate the integrity of cytoplasmic and lysosomal membranes when the cells were exposed to the AuNRs and the free ligands. We used macrophages (dTHP-1) to evaluate the cytotoxicity of both the ligand-coated AuNRs and ligands. Based on the CCK-8 assay, both CTAB and CTAB-Au induced concentration-dependent cytotoxicity. On the contrary, PDC and PDC-Au had negligible effects on cell viability even at high concentrations (Figure 5c). Furthermore, the amount of intracellular NPs is considered as a determinant factor for biological effects. Hence we studied the uptake of NPs by macrophages after incubation with 10 μ g/mL AuNRs for 3, 6, 12, and 24 h. ICP-MS results show that the uptake of both CTAB-Au and PDC-Au is time-dependent; however, more PDC-Au was endocytosed than CTAB-Au (Figure 5d). This was partly due to the difference in the amount of serum proteins adsorbed on the two types of NPs.35 Although more PDC-Au was endocytosed, it induced negligible cytotoxicity and little damage to the membrane.

To verify the influence of NPs on cell membrane integrity, we exposed macrophages to the ligands or the ligand-coated AuNRs in a serum-free culture medium and then measured the released lactate dehydrogenase (LDH) in the medium (Figure 5e). The

results of the LDH assay showed that both CTAB and CTAB-Au increased the cytoplasmic membrane permeability, but CTAB-Au had a stronger effect than CTAB. Compared with the negative control, PDC caused only slight damage to the cell membrane, while PDC-Au did not affect the membrane permeability. These results were consistent with the XRR measurements.

Next, we monitored the structural integrity of the lysosomal membrane upon exposure to the AuNRs. Lysosome is one of the major organelles where NPs are deposited when they enter the cell. Inside the lysosome, the coated proteins on the NPs are removed such that the coating ligands are exposed to the lysosomal membrane.³⁶ Herein, a pH-sensitive probe, acridine orange (AO), was used to detect lysosomal membrane permeability (LMP), and the fluorescence intensity of the macrophages was measured by flow cytometry (Figure 5f). AO exhibits red fluorescence in acidic lysosomes; however, the color changes from red to green when the pH value becomes neutral.³⁴ Both CTAB and CTAB-Au significantly increased LMP in a concentration-dependent manner, but CTAB-Au caused higher permeability than CTAB, which suggested that both the free ligand and CTAB-Au induce membrane damage. In contrast, LMP increased only slightly as the concentration of PDC increased, and PDC at 0.05 μ g/mL had negligible effects on LMP (data not shown). Similarly, PDC-Au did not cause membrane damage even at 10 µg/mL. Comparing CTAB and PDC, both decreased the integrity of the lysosomal membrane at the concentration of 0.5 $\mu g/mL$; however, CTAB caused more severe damage than PDC. The cells treated with polyethylenimine (PEI) were used as the positive control. PEI exhibits considerable buffer capacity in lysosomes, which leads to lysosome swelling and potential rupture of the lysosomal



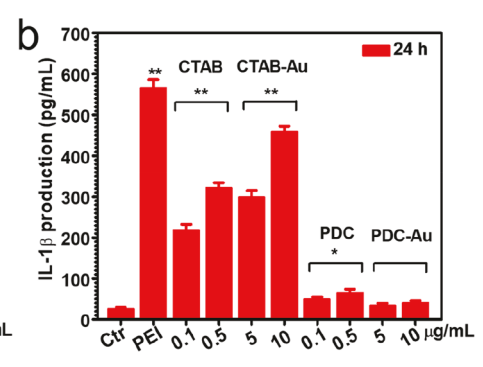


Figure 7. Effects of ligand stability on the inflammatory responses of macrophages. (a, b) Inflammation probed with IL-1 β expression at (a) the mRNA level and at (b) the protein level. Data are the average of four independent replicates. Error bars represent the standard errors. The significant difference between the sample and the control at p < 0.05 is indicated by a single asterisk and that at p < 0.01 by a double asterisk.

membrane, resulting in high LMP. 37,38 At 2 μ g/mL, PEI caused strong LMP, where the pH values changed from acidic to neutral. We further observed the structure of the lysosomal membrane after treatment with the AuNRs by confocal microscopic imaging for AO (Figure 5g). The imaging results showed red fluorescence (vesicular structures) in untreated (control) and the PDC-Au-treated cells, indicating intact lysosomal membranes. After PEI or CTAB-Au treatment, the red fluorescence signals were replaced by green or yellow fluorescences, suggesting an increase in pH and a decrease in membrane integrity. In addition to AO, we used the Magic Red assay, which is not pH dependent, to detect lysosomal membrane integrity (Figure 5h). Magic Red cathepsin B substrate was used to stain the cells. If the lysosomal membrane is damaged, cathepsin B, a lysosomal enzyme, will be released from the lysosome to the cytoplasm, where the enzyme will convert the nonfluorescent substrates to the product with strong red fluorescence signals that is detectable by light microscopic imaging. The imaging results again showed that CTAB-Au rather than PDC-Au impaired the lysosomal membrane. Together, flow cytometry and imaging provided evidence that CTAB-Au increases the lysosomal membrane permeability.

Furthermore, we observed intracellular locations of CTAB-Au and PDC-Au by TEM. After 3 h of uptake, most CTAB-Au was found in the endosomes, lysosomes, and phagosomes (Figure 6c,d). However, after 6 and 24 h, some CTAB-Au was found in the cytoplasm (Figure 6e–h). The result that CTAB-Au was released from lysosomes/endosomes into the cytoplasm also supported the argument that CTAB-Au had damaged the lysosomal membrane and the observations in the AO and Magic Red imaging (Figure 5g and h). Conversely, PDC-Au remained in the endosomes, lysosomes, and phagosomes after 6 and 24 h of uptake (Figure 6i–l), which suggested negligible effects of PDC-Au on the lysosomal membrane integrity. In conclusion, the intracellular location of AuNRs explains the distinct effects of CTAB-Au and PDC-Au on the structure of the lysosomal membrane.

Proinflammatory Effect of AuNRs Due to Low Stability of Surface Ligands. We further evaluated the inflammatory response following the change in the lysosomal membrane permeability triggered by the ligand-coated AuNRs and the free ligands using RT-PCR and ELISA. The increased permeability of the lysosomal membrane may promote the release of proteolytic enzymes and cathepsins from the lysosome to the cytoplasm, which is highly correlated with the activation of inflammation, as well as the maturation and the secretion of proinflammatory cytokines such as IL-1 β . At the mRNA level,

macrophages highly expressed IL-1 β after exposure to PEI, CTAB, and CTAB-Au, which show a time- and concentration-dependent response. Compared with CTAB and CTAB-Au, PDC and PDC-Au induced much less change in the mRNA expression (Figure 7a). At the protein level, a similar trend was observed. Based on ELISA, PEI, CTAB, and CTAB-Au significantly promoted the secretion of IL-1 β . Particularly, after exposure to 5 and 10 μ g/mL CTAB-Au for 24 h, the amounts of secreted IL-1 β were increased by about 10-fold and 16-fold, respectively. The secretion of IL-1 β increased only slightly by PDC and had a negligible change by PDC-Au (Figure 7b).

Therefore, the inflammation induced by the ligand-coated AuNRs was directly correlated with the integrity of the lysosomal membrane, which was largely due to the stability of surface ligands on the AuNRs. Both ligands and CTAB-Au induced inflammation due to their interactions with the lysosomal membrane and the subsequent change in the membrane structure. Moreover, CTAB-Au triggered a stronger inflammatory response than CTAB, while at the same concentrations PDC-Au did not promote inflammation due to negligible effects on the lysosomal membrane structure. That is to say, cationic surfactant-coated NPs (CTAB-Au) induced much stronger inflammation than polyelectrolyte-coated ones (PDC-Au) due to distinct interactions of ligands with the lysosomal membrane and the subsequent change in the membrane structures.

Based on our findings, strategies to anchor ligands on the surface of NPs are thus important for biomedical applications. For example, the conjugation of PEI and other polymers to NPs can significantly reduce the acute toxicity induced by free PEI³⁷ and increase transfection capability. ^{40,41} In addition, to reduce the toxicity of cationic surfactant-coated NPs, the surfactant molecules can be either coated by layered polyelectrolytes²⁹ or stabilized by polymerization, cross-linking, ¹³ and other chemical modifications for better adsorption. ⁴²

CONCLUSIONS

In summary, combining X-ray liquid surface scattering techniques with MD simulations, we have uncovered the mechanism of membrane structural change due to the different self-assembled structures and the stability of the coating ligands on AuNRs. In the CTAB-Au system, the CTA molecules form a bilayer structure on the surface of AuNRs, while the binding affinity between CTA and CTAB-Au is low. As a result, when CTAB-Au is in contact with the membrane surface, some CTA molecules may detach from the CTAB bilayer. The released

CTA molecules may intercalate into the membrane and cause a decrease in the membrane thickness. The resulting change in the membrane structure is directly associated with cytotoxicity and inflammatory responses. In constrast, in the PDC-Au system, the PDC molecules are stable on the surface of AuNRs and have negligible effects on the membrane thickness, cytotoxicity, and inflammation. Together, our study provides structural aspects of the important contribution of ligand stability on the surface of NPs to the modulation of nanotoxicity and inflammatory responses. To the best of our knowledge, this is a direct observation of the transfer of unstable ligands released from the surface of membrane-bound NPs to the phospholipid layer. Our results support the engineering of NPs to release surface coating molecules onto membranes for functional design. It is therefore important to consider the properties of coating ligands and the structures of bio-nano interfaces when we explore the biological effects of NPs. The applied quantitative analysis of the interface structures also helps explore the interaction between NPs and biological systems, which has promising applications for both nanosafety assessment and rational design of NPs in the future.

MATERIALS AND METHODS

Preparation of Ligand-Coated AuNRs. CTAB-Au and PDC-Au were prepared according to previous publications.²⁹ CTAB-Au is a pristine AuNR coated with a CTAB bilayer. PDC-Au is a pristine AuNR with three surface coatings, including a CTAB bilayer, which makes up the innermost layer, followed by PSS in the middle layer, followed by PDC in the outermost layer. Figure S1 shows the structural formulas of the three coating ligands and a schematic diagram of this layer-by-layer deposition process of the ligands on the surface of a AuNR. The concentrations of the stock solutions of the Au elements and the CTAB and PDC were 100 μ g/mL, 36.4 mg/mL (0.1 M), and 5 mg/mL, respectively. About 50 mL of the CTAB-Au and PDC-Au dispersions were each centrifuged twice at 9000 rpm for 10 min to remove the excess ligands in the supernatant. After the first centrifugation, about 0.25 mL of the supernatant remained and 49.75 mL of water was added. Then, the second centrifugation was done, and 0.25 mL of supernatant was left to disperse AuNRs. The final concentration of AuNRs was 20 mg/mL, while the concentrations of CTAB and PDC were approximately 0.18 mg/mL and 25 µg/mL, respectively. For the following experiments, the concentrations of the AuNRs were diluted to 10 μ g/mL, while those of the free CTAB and PDC were ~0.11 μ g/mL and ~12.5 ng/mL, respectively.

Characterization of Ligand-Coated AuNRs. The diluted ligandcoated AuNRs at 100 μ g/mL were then placed on copper grids and dried for TEM imaging (FEI Tecnai F-20) to record the sizes and shapes. The surface charges were measured using 50 μ g/mL of the ligand-coated AuNRs in deionized water before and after incubation with fetal bovine serum by a zeta potential and dynamic size analyzer (Malvern Zeta Sizer Nano ZS). For the serum incubation, the ligandcoated AuNRs were each added in a cell culture medium containing 10% fetal bovine serum for 30 min. Then the dispersions were centrifuged at 9000 rpm for 10 min, and the precipitates were suspended in water before zeta potential measurement. The thermodynamics parameters for the interaction of CTAB and PDC with the corresponding ligand-coated AuNRs were measured by ITC at 37 °C. In total, 250 μ L of 0.7 mM CTAB was titrated into 1 mL of 3.5 nM CTAB-Au in water, and 250 μ L of 0.5 mM PDC was titrated into 1 mL of 50.25 nM PSS-Au in water.

X-ray Reflectivity and Grazing Incidence X-ray Off-Specular Scattering. XRR and GIXOS were employed on a liquid surface reflectometer on the ChemMatCARS 15-ID-C beamline at the Advanced Photon Source at Argonne National Laboratory. 43,44 The energy of incident X-rays was 10 keV with a wavelength of 1.238 94 Å. A 60 mL single-barrier Langmuir trough with dimensions of $7.78 \text{ } (W) \times 17.8 \text{ } (L) \times 0.3 \text{ } (H) \text{ cm}^3 \text{ was used for the } in \text{ situ} \text{ XRR} \text{ and GIXOS}$ experiments. As the ligand-coated AuNRs tend to aggregate in

phosphate-buffered saline (PBS), pure water was used to mitigate the aggregation. A SOPC monolayer was spread on the surface of water. A target surface pressure of 20 mN/m was maintained to be similar to the physiological states of most biological membranes. Either CTAB-Au or PDC-Au dispersion was injected into the subphase, which was continuously stirred for 40 min at 120 rpm with a Teflon-coated magnetic bar to disperse the nanoparticles and to improve their adsorption to SOPC. Then, the reflectivity was measured by a two-dimensional hybrid pixel array X-ray detector (PILATUS 100 K). The final concentrations of the ligand-coated AuNRs were 5 and 10 μ g/mL. To keep the same amount of the quaternary ammonium groups as that in CTAB, the corresponding concentrations of PDC were 0.05, 0.25, and 0.5 μ g/mL, respectively.

XRR measures the intensity of the reflected X-ray as a function of incident angle, α , with respect to the plane of the liquid surface in the specular condition. A schematic diagram of the experimental setup and the scattering geometry is illustrated in Figure 1d. Q_z is the component of the wavevector transfer of the reflected X-rays, \vec{Q} , in the z-direction normal to the surface. The relationship between Q_z and α is given by eq

$$Q_z = (4\pi/\lambda)\sin(\alpha) \tag{1}$$

The reflectivity, $R(Q_z)$, is the intensity of the reflected X-rays normalized by the intensity of the incident X-rays. $R(Q_z)$ is often normalized by Fresnel reflectivity, $R_F(Q_z)$, which is a theoretical reflectivity for an ideal flat abrupt interface between vacuum and a bulk phase. The deviations of $R(Q_z)$ from $R_F(Q_z)$, the $R(Q_z)/R_F(Q_z)$ values, were analyzed to obtain the electron density profile of the interface normal to the surface by the slab model 32,47 with the Parratt recursive algorithm. After data collection, XRR data were analyzed and the best fits of the data were obtained based on a model-dependent and iterative fitting procedure.

In GIXOS, incident X-rays at a fixed angle (α = 0.1016°) were used. The incident angle was below the critical angle of the subphase (α_c = 0.123°) for total external reflection. The GIXOS data were collected simultaneously at a wide range of scattering angles, β , from 0° to 7.5°, which covered Q_c from 0.01 to 0.658 Å⁻¹, with an azimuthal angle θ of 0.3°. The detector was placed 550 mm downstream of the sample. The GIXOS experimental setup and the background measurements have been described in detail in a previous study.

Slab Model. The average electron density distribution along the surface normal, $\langle \rho(z) \rangle$, describes the interface structure and is related to the specular X-ray reflectivity, $R(Q_z)$, in the "master formula". Due to taking the absolute value of the integral of $\langle \rho(z) \rangle$, all information on the phase is lost. To recover $\langle \rho(z) \rangle$, a model of $\rho(z)$ is numerically fitted to the measured values of $R(Q_z)$.

The model is constructed by a sum of error functions.

$$\rho(z) = \frac{1}{2} \sum_{i=1}^{N+1} \text{erf} \left(\frac{z - z_i}{\sqrt{2} \sigma_i} \right) (\rho_i - \rho_{i+1}) + \frac{\rho_{\text{water}}}{2}$$

where $\operatorname{erf}(z) = 2/\sqrt{\pi} \int_0^z \mathrm{d}t$, N+1 is the number of interfaces, ρ_i is the electron density of slab i with $\rho_{N+2} = 0$ and $\rho_{\text{water}} = 0.333 \, \mathrm{e/\mathring{A}}^3$, and z_i and σ_i are the position and roughness of interface i, respectively. The thickness of slab i is defined as $|z_{i+1} - z_i|$.

Molecular System Setup. To simulate the interactions of CTAB-Au and PDC-Au with a SOPC bilayer, we considered the interactions between the coating ligands of AuNRs and the lipids. Compared with CTAB, the Au atoms of CTAB-Au are relatively distant from the lipids and their contributions to the interactions are small and therefore neglected (but to be consistent with the naming in the experiments above, we still called it "CTAB-Au"). Similarly, the Au atoms of "PDC-Au" were also neglected. Essentially, AuNRs provided an anchor for the CTAB and PDC layered structures.

The SOPC bilayer was generated by the Membrane Builder of CHARMM-GUI 47 with dimensions of 80 Å \times 80 Å. The CTAB bilayer was made of a total of 312 CTA, with 156 CTA at each leaflet. The size of the CTAB bilayer was 79 Å \times 70 Å. The PDDA layer consisted of a

total of 182 DDA with dimensions of 76 Å \times 73 Å. When constructing the initial system of CTAB-Au, we placed the CTAB bilayer at two different distances from the surface of the SOPC bilayer; the minimum distances between the two bilayers were 0.23 Å (Figure S9) and 7.23 Å (Figure 3a), respectively. Likewise, for the PDC-Au system, we placed the PDDA layer above the membrane surface; the minimum distance between the PDDA layer and the lipid bilayer was 1.16 Å. To prevent the PDDA layer from moving away from the membrane surface in the simulations due to lack of anchoring from the inner coating ligands or AuNRs, we added the CTAB bilayer on top of the PDDA layer along the z-axis for the structural support. The minimum distance between the CTAB bilayer and the membrane was 8.73 Å.

To assess the effect of inserted CTA on the thickness of the SOPC bilayer, we constructed heterogeneous membrane systems of a SOPC bilayer with four different concentrations of inserted CTA, 0%, 10%, 20%, and 50%. The systems were first generated by the Membrane Builder of CHARMM-GUI 47 using SOPC lipids and stearic acids with the following compositions: 100% SOPC, 90% SOPC + 10% stearic acid, 80% SOPC + 20% stearic acid, and 50% SOPC + 50% stearic acid. Then for each system, we mutated the stearic acids to CTA. The system sizes were around 80 Å × 80 Å.

Molecular Dynamics Simulation. The two CTAB-Au systems and one PDC-Au system constructed above were each solvated in the center of an $80~\text{Å} \times 80~\text{Å} \times 115~\text{Å}$ water box. For each of the two CTAB-Au systems, 312 water molecules were replaced by 312 bromide ions, while for the PDC-Au system, 182 water molecules were replaced by 182 chloride ions. The resulting systems were neutralized with counterions and ionized with 150 mM NaCl. The initial setups for the three systems are shown in Figures 3 and S9.

Each of the three systems was subjected to 12 000 steps of energy minimization, followed by a 1.2 ns equilibration with a harmonic restraint on the phosphorus atoms of SOPC and the nitrogen atoms of CTA. The force constant was 1 kcal/mol/Ų. After the first equilibration, a harmonic restraint with a force constant of 0.1 kcal/mol/Ų was applied to the same selected atoms. The systems were equilibrated again for 1.2 ns. Finally, the restraints were relieved, and a 300 ns trajectory was generated for each system in a production run.

Similarly, the four heterogeneous membrane systems (100% SOPC, 90% SOPC + 10% CTA, 80% SOPC + 20% CTA, and 50% SOPC + 50% CTA) were each solvated in the center of an 80 Å × 80 Å × 80 Å water box. For the 10% CTA system, 22 water molecules were replaced by 22 bromide ions; for the 20% CTA system, 44 water molecules were replaced; for the 50% CTA system, 134 water molecules were replaced. The resulting systems were then neutralized with counterions and ionized with 150 mM NaCl. Again, each of the four systems was minimized and equilibrated as described above before a 100 ns production run. For the 50% CTA system, three independent trajectories were performed.

All MD simulations were performed by the NAMD program ⁴⁹ in the NPT ensemble at 1 atm and 310 K with a time step of 2 fs. In the two equilibration runs, the area of the unit cell in the x-y planes was kept constant, while in the production run, the ratio of the unit cell in the x-y planes was kept constant. The CHARMM36 force field ⁵⁰ and TIP3P water model ⁵¹ were used. The Lennard-Jones parameters for bromide ions were taken from a previous study. ⁵² The nonbonding interactions were calculated with a typical cutoff distance of 12 Å, while the longrange electrostatic interactions were enumerated with the Particle Mesh Ewald algorithm. ⁵³ For the two CTAB-Au systems and one PDC-Au system, we performed six independent trajectories each.

ASSOCIATED CONTENT

S Supporting Information

The Supporting Information is available free of charge on the ACS Publications website at DOI: 10.1021/acsnano.9b00114.

Characterization results for CTAB-Au and PDC-Au, results of XRR and GIXOS, ITC results for the binding between ligands and AuNRs, structure of the SOPC bilayer by computation (PDF)

Movie for MD simulations of the dynamic interactions between three CTA ligands on AuNRs and a SOPC bilayer (AVI)

Movie for MD simulations of the dynamic interactions between one CTA ligand on AuNRs and a SOPC bilayer (AVI)

Movie for MD simulations of the dynamic interactions between PDDA ligands on AuNRs and a SOPC bilayer (AVI)

AUTHOR INFORMATION

Corresponding Authors

*E-mail: lin@cars.uchicago.edu. *E-mail: ruhongz@us.ibm.com. *E-mail: chenchy@nanoctr.cn.

ORCID ®

Liming Wang: 0000-0003-1382-9195 Yu-Feng Li: 0000-0002-5013-5849 Yuliang Zhao: 0000-0002-9586-9360 Binhua Lin: 0000-0001-5932-4905 Ruhong Zhou: 0000-0001-8624-5591 Chunying Chen: 0000-0002-6027-0315

Author Contributions

[#]L. Wang, P. Quan, and S. H. Chen contributed equally.

Notes

The authors declare no competing financial interest.

ACKNOWLEDGMENTS

This work was supported by the Ministry of Science and Technology of China (2016YFA0201600, 2016YFA0203200), Key Program for International S&T Cooperation Projects of China (2016YFE0133100), the National Natural Science Foundation of China (91543206, 11435002, 11574224), Science Fund for Creative Research Groups of the National Natural Science Foundation of China (11621505), the National Science Fund for Distinguished Young Scholars (11425520), CAS Key Research Program for Frontier Sciences (QYZDJ-SSW-SLH022), and the CAS Interdisciplinary Innovation Team. We appreciate the assistance by BL07W in NSRL and the Users with Excellence Project of Hefei Science Center CAS (2018HSC-UE004). A part of this work was supported by NSF's ChemMatCARS Sector 15, which is supported by the Divisions of Chemistry (CHE) and Materials Research (DMR), National Science Foundation, under grant number NSF/CHE-1834750. Use of the Advanced Photon Source, an Office of Science User Facility operated for the U.S. Department of Energy (DOE) Office of Science by Argonne National Laboratory, was supported by the U.S. DOE under Contract No. DE-AC02-06CH11357. B.L. acknowledges the support from the University of Chicago MRSEC under grant number NSF/DMR-1420709. R.Z. acknowledges the support from IBM Blue Gene Science Program (W125859, W1464125, and W1464164).

REFERENCES

- (1) Kuna, J. J.; Voitchovsky, K.; Singh, C.; Jiang, H.; Mwenifumbo, S.; Ghorai, P. K.; Stevens, M. M.; Glotzer, S. C.; Stellacci, F. The Effect of Nanometre-Scale Structure on Interfacial Energy. *Nat. Mater.* **2009**, *8*, 837–842.
- (2) Daniel, M. C.; Astruc, D. Gold Nanoparticles: Assembly, Supramolecular Chemistry, Quantum-Size-Related Properties, and Applications Toward Biology, Catalysis, and Nanotechnology. *Chem. Rev.* **2004**, *104*, 293–346.

(3) Chen, S. H.; Kang, S. G.; Luo, J. D.; Zhou, R. H. Charging Nanoparticles: Increased Binding of Gd@C82(OH)(22) Derivatives to Human MMP-9. *Nanoscale* **2018**, *10*, 5667–5677.

- (4) Wang, L.; Jiang, X.; Ji, Y.; Bai, R.; Zhao, Y.; Wu, X.; Chen, C. Surface Chemistry of Gold Nanorods: Origin of Cell Membrane Damage and Cytotoxicity. *Nanoscale* **2013**, *5*, 8384–8391.
- (5) Walkey, C. D.; Olsen, J. B.; Guo, H. B.; Emili, A.; Chan, W. C. W. Nanoparticle Size and Surface Chemistry Determine Serum Protein Adsorption and Macrophage Uptake. *J. Am. Chem. Soc.* **2012**, *134*, 2139–2147.
- (6) Verma, A.; Uzun, O.; Hu, Y. H.; Hu, Y.; Han, H. S.; Watson, N.; Chen, S. L.; Irvine, D. J.; Stellacci, F. Surface-Structure-Regulated Cell-Membrane Penetration by Monolayer-Protected Nanoparticles. *Nat. Mater.* **2008**, *7*, 588–595.
- (7) Jana, N. R.; Gearheart, L.; Murphy, C. J. Seed-Mediated Growth Approach for Shape-Controlled Synthesis of Spheroidal and Rod-Like Gold Nanoparticles Using a Surfactant Template. *Adv. Mater.* **2001**, *13*, 1389–1393.
- (8) Wang, X.; Wang, M.; Lei, R.; Zhu, S. F.; Zhao, Y.; Chen, C. Chiral Surface of Nanoparticles Determines the Orientation of Adsorbed Transferrin and Its Interaction with Receptors. *ACS Nano* **2017**, *11*, 4606–4616.
- (9) Lesniak, A.; Salvati, A.; Santos-Martinez, M. J.; Radomski, M. W.; Dawson, K. A.; Aberg, C. Nanoparticle Adhesion to the Cell Membrane and Its Effect on Nanoparticle Uptake Efficiency. *J. Am. Chem. Soc.* **2013**, *135*, 1438–1444.
- (10) Luo, N. N.; Weber, J. K.; Wang, S.; Luan, B. Q.; Yue, H.; Xi, X. B.; Du, J.; Yang, Z. X.; Wei, W.; Zhou, R. H.; Ma, G. H. PEGylated Graphene Oxide Elicits Strong Immunological Responses Despite Surface Passivation. *Nat. Commun.* **2017**, *8*, 14537.
- (11) Wang, L.; Li, J.; Pan, J.; Jiang, X.; Ji, Y.; Li, Y.; Qu, Y.; Zhao, Y.; Wu, X.; Chen, C. Revealing the Binding Structure of the Protein Corona on Gold Nanorods Using Synchrotron Radiation-Based Techniques: Understanding the Reduced Damage in Cell Membranes. *J. Am. Chem. Soc.* **2013**, *135*, 17359–17368.
- (12) Ge, C.; Du, J.; Zhao, L.; Wang, L.; Liu, Y.; Li, D.; Yang, Y.; Zhou, R.; Zhao, Y.; Chai, Z.; Chen, C. Binding of Blood Proteins to Carbon Nanotubes Reduces Cytotoxicity. *Proc. Natl. Acad. Sci. U. S. A.* **2011**, 108, 16968–16973.
- (13) Alkilany, A. M.; Murphy, C. J. Gold Nanoparticles with a Polymerizable Surfactant Bilayer: Synthesis, Polymerization, and Stability Evaluation. *Langmuir* **2009**, *25*, 13874–13879.
- (14) Kvitek, L.; Panacek, A.; Soukupova, J.; Kolar, M.; Vecerova, R.; Prucek, R.; Holecova, M.; Zboril, R. Effect of Surfactants and Polymers on Stability and Antibacterial Activity of Silver Nanoparticles. *J. Phys. Chem. C* **2008**, *112*, 5825–5834.
- (15) Gomez-Grana, S.; Hubert, F.; Testard, F.; Guerrero-Martinez, A.; Grillo, I.; Liz-Marzan, L. M.; Spalla, O. Surfactant (bi)Layers on Gold Nanorods. *Langmuir* **2012**, *28*, 1453–1459.
- (16) Hochmuth, R. M.; Evans, E. A.; Wiles, H. C.; Mccown, J. T. Mechanical Measurement of Red-Cell Membrane Thickness. *Science* 1983, 220, 101–102.
- (17) Leroueil, P. R.; Hong, S.; Mecke, A.; Baker, J. R., Jr; Orr, B. G.; Banaszak Holl, M. M. Nanoparticle Interaction with Biological Membranes: Does Nanotechnology Present a Janus Face? *Acc. Chem. Res.* **2007**, *40*, 335–342.
- (18) Xiao, M. Y.; Jasensky, J.; Foster, L.; Kuroda, K.; Chen, Z. Monitoring Antimicrobial Mechanisms of Surface-Immobilized Peptides *In Situ. Langmuir* **2018**, *34*, 2057–2062.
- (19) Koulov, A. V.; Lambert, T. N.; Shukla, R.; Jain, M.; Boon, J. M.; Smith, B. D.; Li, H. Y.; Sheppard, D. N.; Joos, J. B.; Clare, J. P.; Davis, A. P. Chloride Transport Across Vesicle and Cell Membranes by Steroid-Based Receptors. *Angew. Chem., Int. Ed.* **2003**, *42*, 4931–4933.
- (20) Gidalevitz, D.; Ishitsuka, Y. J.; Muresan, A. S.; Konovalov, O.; Waring, A. J.; Lehrer, R. I.; Lee, K. Y. C. Interaction of Antimicrobial Peptide Protegrin with Biomembranes. *Proc. Natl. Acad. Sci. U. S. A.* **2003**, *100*, 6302–6307.
- (21) Wu, L.; Zeng, L.; Jiang, X. E. Revealing the Nature of Interaction Between Graphene Oxide and Lipid Membrane by Surface-Enhanced

Infrared Absorption Spectroscopy. J. Am. Chem. Soc. 2015, 137, 10052–10055.

- (22) Málková, Š.; Long, F.; Stahelin, R. V.; Pingali, S. V.; Murray, D.; Cho, W.; Schlossman, M. L. X-Ray Reflectivity Studies of cPLA2α-C2 Domains Adsorbed onto Langmuir Monolayers of SOPC. *Biophys. J.* **2005**, *89*, 1861–1873.
- (23) Tietjen, G. T.; Gong, Z.; Chen, C. H.; Vargas, E.; Crooks, J. E.; Cao, K. D.; Heffern, C. T. R.; Henderson, J. M.; Meron, M.; Lin, B.; Roux, B.; Schlossman, M. L.; Steck, T. L.; Lee, K. Y. C.; Adams, E. J. Molecular Mechanism for Differential Recognition of Membrane Phosphatidylserine by the Immune Regulatory Receptor Tim4. *Proc. Natl. Acad. Sci. U. S. A.* 2014, 111, E1463–1472.
- (24) Martynowycz, M. W.; Hu, B.; Kuzmenko, I.; Bu, W.; Hock, A.; Gidalevitz, D. Monomolecular Siloxane Film as a Model of Single Site Catalysts. *J. Am. Chem. Soc.* **2016**, *138*, 12432–12439.
- (25) Cristofolini, L. Synchrotron X-Ray Techniques for the Investigation of Structures and Dynamics in Interfacial Systems. *Curr. Opin. Colloid Interface Sci.* **2014**, *19*, 228–241.
- (26) Dai, Y.; Lin, B.; Meron, M.; Kim, K.; Leahy, B.; Shpyrko, O. G. A Comparative Study of Langmuir Surfactant Films: Grazing Incidence X-Ray Off-Specular Scattering vs. X-Ray Specular Reflectivity. *J. Appl. Phys.* **2011**, *110*, 102213.
- (27) Jimenez-Cruz, C. A.; Kang, S. G.; Zhou, R. H. Large Scale Molecular Simulations of Nanotoxicity. *Wires Syst. Biol. Med.* **2014**, *6*, 265–279.
- (28) Nikoobakht, B.; El-Sayed, M. A. Evidence for Bilayer Assembly of Cationic Surfactants on the Surface of Gold Nanorods. *Langmuir* **2001**, *17*, 6368–6374.
- (29) Gole, A.; Murphy, C. J. Polyelectrolyte-Coated Gold Nanorods: Synthesis, Characterization and Immobilization. *Chem. Mater.* **2005**, 17, 1325–1330.
- (30) Ross, P. D.; Subramanian, S. Thermodynamics of Protein Association Reactions-Forces Contributing to Stability. *Biochemistry* **1981**, 20, 3096–3102.
- (31) Bera, M. K.; Qiao, B. F.; Seifert, S.; Burton-Pye, B. P.; de la Cruz, M. O.; Antonio, M. R. Aggregation of Heteropolyanions in Aqueous Solutions Exhibiting Short-Range Attractions and Long-Range Repulsions. *J. Phys. Chem. C* **2016**, *120*, 1317–1327.
- (32) Bu, W.; Vaknin, D.; Travesset, A. How Accurate Is Poisson-Boltzmann Theory for Monovalent Ions near Highly Charged Interfaces? *Langmuir* **2006**, *22*, 5673–5681.
- (33) Wang, B.; Zhang, L. F.; Bae, S. C.; Granick, S. Nanoparticle-Induced Surface Reconstruction of Phospholipid Membranes. *Proc. Natl. Acad. Sci. U. S. A.* **2008**, *105*, 18171–18175.
- (34) Li, J. Y.; Das, P.; Zhou, R. H. Single Mutation Effects on Conformational Change and Membrane Deformation of Influenza Hemagglutinin Fusion Peptides. *J. Phys. Chem. B* **2010**, *114*, 8799–8806.
- (35) Qiu, Y.; Liu, Y.; Wang, L.; Xu, L.; Bai, R.; Ji, Y.; Wu, X.; Zhao, Y.; Li, Y.; Chen, C. Surface Chemistry and Aspect Ratio Mediated Cellular Uptake of Au Nanorods. *Biomaterials* **2010**, *31*, 7606–7619.
- (36) Chanana, M.; Gil, P. R.; Correa-Duarte, M. A.; Liz-Marzan, L. M.; Parak, W. J. Physicochemical Properties of Protein-Coated Gold Nanoparticles in Biological Fluids and Cells Before and After Proteolytic Digestion. *Angew. Chem., Int. Ed.* **2013**, *52*, 4179–4183.
- (37) Parhamifar, L.; Larsen, A. K.; Hunter, A. C.; Andresen, T. L.; Moghimi, S. M. Polycation Cytotoxicity: A Delicate Matter for Nucleic Acid Therapy-Focus on Polyethylenimine. *Soft Matter* **2010**, *6*, 4001–4009
- (38) Wang, L.; Liu, Y.; Li, W.; Jiang, X.; Ji, Y.; Wu, X.; Xu, L.; Qiu, Y.; Zhao, K.; Wei, T.; Zhao, Y.; Chen, C. Selective Targeting of Gold Nanorods at the Mitochondria of Cancer Cells: Implications for Cancer Therapy. *Nano Lett.* **2011**, *11*, 772–780.
- (39) Henao-Mejia, J.; Elinav, E.; Strowig, T.; Flavell, R. A. Inflammasomes: Far Beyond Inflammation. *Nat. Immunol.* **2012**, *13*, 321–324.
- (40) Xu, L.; Liu, Y.; Chen, Z.; Li, W.; Liu, Y.; Wang, L.; Liu, Y.; Wu, X.; Ji, Y.; Zhao, Y.; Ma, L.; Shao, Y.; Chen, C. Surface-Engineered Gold

Nanorods: Promising DNA Vaccine Adjuvant for HIV-1 Treatment. *Nano Lett.* **2012**, *12*, 2003–2012.

- (41) Brownlie, A.; Uchegbu, I. F.; Schatzlein, A. G. PEI-Based Vesicle-Polymer Hybrid Gene Delivery System with Improved Biocompatibility. *Int. J. Pharm.* **2004**, 274, 41–52.
- (42) Vigderman, L.; Manna, P.; Zubarev, E. R. Quantitative Replacement of Cetyl Trimethylammonium Bromide by Cationic Thiol Ligands on the Surface of Gold Nanorods and Their Extremely Large Uptake by Cancer Cells. *Angew. Chem., Int. Ed.* **2012**, *51*, 636–641.
- (43) Pershan, P. S. Effects of Thermal Roughness on X-Ray Studies of Liquid Surfaces. *Colloids Surf., A* **2000**, *171*, 149–157.
- (44) Schlossman, M. L.; Synal, D.; Guan, Y. M.; Meron, M.; Shea-McCarthy, G.; Huang, Z. Q.; Acero, A.; Williams, S. M.; Rice, S. A.; Viccaro, P. J. A Synchrotron X-Ray Liquid Surface Spectrometer. *Rev. Sci. Instrum.* 1997, 68, 4372–4384.
- (45) Knoll, G. F. Radiation Detection and Measurement, 4th ed.; John Wiley & Sons, Inc.: New York, 2010; pp 25–33.
- (46) Meron, M.; Gebhardt, J.; Brewer, H.; Viccaro, J. P.; Lin, B. Following Transient Phases at the Air/Water Interface. *Eur. Phys. J.: Spec. Top.* **2009**, *167*, 137–142.
- (47) Bu, W.; Yu, H.; Luo, G. M.; Bera, M. K.; Hou, B. Y.; Schuman, A. W.; Lin, B. H.; Meron, M.; Kuzmenko, I.; Antonio, M. R.; Soderholm, L.; Schlossman, M. L. Observation of a Rare Earth Ion-Extractant Complex Arrested at the Oil Water Interface During Solvent Extraction. *J. Phys. Chem. B* **2014**, *118*, 10662–10674.
- (48) Parratt, L. G. Surface Studies of Solids by Total Reflection of X-Rays. *Phys. Rev.* **1954**, *95*, 359–369.
- (49) Phillips, J. C.; Braun, R.; Wang, W.; Gumbart, J.; Tajkhorshid, E.; Villa, E.; Chipot, C.; Skeel, R. D.; Kale, L.; Schulten, K. Scalable Molecular Dynamics with NAMD. J. Comput. Chem. 2005, 26, 1781–1802.
- (50) Klauda, J. B.; Venable, R. M.; Freites, J. A.; O'Connor, J. W.; Tobias, D. J.; Mondragon-Ramirez, C.; Vorobyov, I.; MacKerell, A. D.; Pastor, R. W. Update of the Charmm All-Atom Additive Force Field for Lipids: Validation on Six Lipid Types. *J. Phys. Chem. B* **2010**, *114*, 7830–7843.
- (51) Jorgensen, W. L.; Chandrasekhar, J.; Madura, J. D.; Impey, R. W.; Klein, M. L. Comparison of Simple Potential Functions for Simulating Liquid Water. *J. Chem. Phys.* **1983**, *79*, 926–935.
- (52) Lybrand, T. P.; Ghosh, I.; Mccammon, J. A. Hydration of Chloride and Bromide Anions: Determination of Relative Free-Energy by Computer Simulation. *J. Am. Chem. Soc.* **1985**, *107*, 7793–7794.
- (53) Darden, T.; York, D.; Pedersen, L. Particle Mesh Ewald-An N. Log(N) Method for Ewald Sums in Large Systems. *J. Chem. Phys.* **1993**, 98, 10089–10092.